Author Contributions:

Conceptualization: S. A. M. den Hartog, C. Marone, D. M. Saffer
Formal analysis: S. A. M. den Hartog
Methodology: S. A. M. den Hartog
Supervision: C. Marone, D. M. Saffer
Validation: S. A. M. den Hartog, C. Marone, D. M. Saffer
Visualization: S. A. M. den Hartog
Writing – original draft: S. A. M. den Hartog, C. Marone, D. M. Saffer
Writing – review & editing: S. A. M. den Hartog, C. Marone, D. M. Saffer

Frictional Behavior Downdip Along the Subduction Megathrust: Insights From Laboratory Experiments on Exhumed Samples at In Situ Conditions

S. A. M. den Hartog[1,2,3] , **C. Marone[1,4]** , and **D. M. Saffer[5]**

[1]Department of Geosciences, The Pennsylvania State University, University Park, PA, USA, [2]The Lyell Centre, Heriot-Watt University, Edinburgh, UK, [3]Now at State Supervision of Mines, Ministry of Economic Affairs and Climate Policy, The Hague, The Netherlands, [4]Dipartimento di Scienze della Terra, La Sapienza Università di Roma, Rome, Italy, [5]Department of Geological Sciences, Jackson School of Geosciences, Institute for Geophysics, University of Texas, Austin, TX, USA

Abstract Subduction megathrusts exhibit a spectrum of slip modes, including catastrophic earthquakes. Although the mechanical and frictional properties of materials sampled from subduction zones have been studied extensively, few datasets have been collected for compositions and at pressure and temperature conditions representative of those in situ. The Nankai subduction zone in southwest Japan is a well-studied margin, and abundant data provide an opportunity to advance our understanding of fault and earthquake physics. Here, we use samples exhumed in the Shimanto and Sanbagawa Belts on Shikoku Island of southwest Japan that represent analogs for materials along the present-day megathrust at depths of ∼5–>25 km, and we shear these at their peak in situ pressure-temperature (*P-T*) conditions. Effective normal stresses range from 28 to 192 MPa, and temperatures from 105°C to 470°C. We used pore fluid pressures of 45–240 MPa, corresponding to fluid overpressure ratios λ of 0.65 and 0.90. Slip velocities of 0.1–100 μm/s were used, in order to focus on the nucleation of instability and earthquakes. We found predominantly velocity-strengthening (inherently stable) behavior under all conditions for $\lambda = 0.65$. For $\lambda = 0.90$, velocity-weakening behavior was observed at 350°C, with velocity-strengthening behavior at lower and higher temperatures. The rate/state frictional stability parameter (*a-b*) increases with slip velocity at temperatures up to ∼200°C and remains constant or decreases with slip velocity at higher temperatures. Overall, our results demonstrate the potentially important roles of both temperature and slip velocity in controlling the distribution of stress and frictional rheology along subduction thrusts.

Plain Language Summary The largest earthquakes on Earth occur along fault zones at subduction plate boundaries. These earthquakes are controlled, in large part, by the frictional properties of the fault zone materials. However, those properties are not fully understood, and laboratory experiments are key to advancing our knowledge. One example of a subduction zone is the Nankai Trough in southwest Japan. This subduction zone has been the subject of several drilling expeditions, recovering samples from the subsurface, and providing materials used in laboratory experiments. However, the experiments to date focus on materials recovered from depths shallower than those where earthquakes nucleate, and have been performed at temperatures lower than those in earthquake source regions. In this study, we used samples known to come from depths where earthquakes nucleate, and we performed friction experiments at temperatures and pressures relevant for these depths. We find that the frictional properties are primarily dependent on temperature and on the velocity of sliding.

1. Introduction

Subduction zones host the largest and most catastrophic earthquakes on Earth. Nucleation of fast earthquakes (slip rates of ∼0.1–1 m/s; Cowan, 1999) on subduction megathrusts is generally observed to concentrate in a depth range termed "the seismogenic zone" (e.g., Hyndman et al., 1997; Oleskevich et al., 1999). Episodic slow-slip events (SSEs) and quasi-static creep (slip rates of ∼10^{-9}–10^{-7} m/s; Iio et al., 2002; Liu & Rice, 2005) predominantly occur near the updip and downdip limits of this depth window (e.g., Araki et al., 2017; Bilek & Lay, 2018; Kano et al., 2019; Schwartz & Rokosky, 2007; Wallace et al., 2016). There is considerable complexity superimposed on this simple model; for example, both slow slip and creep occur within the seismogenic zone and beyond its boundaries (e.g., Ito et al., 2013), and although nucleation of coseismic slip is generally limited to the

seismogenic zone, dynamic rupture may extend outside this zone and to shallow depths (e.g., Lay, 2018; Lay & Bilek, 2007). Nonetheless, to first order, the depth extent of earthquake nucleation in subduction zones appears to be thermally controlled, with the updip limit occurring at 100°C–150°C and the downdip limit at approximately 350°C–450°C (Hyndman et al., 1997; Moore & Saffer, 2001; Oleskevich et al., 1999).

The Nankai Trough in southwest Japan has repeatedly generated devastating earthquakes, most recently in 1944 and 1946, events known as the Tonankai (M_w 8.1) and Nankaido (M_w 8.3) earthquakes, respectively (Ando, 1975). A spectrum of slow earthquake and slip behavior has also been observed along the subduction thrust here, including tremor, very low-frequency earthquakes and SSEs (e.g., Araki et al., 2017; Hirose & Obara, 2005; Ito et al., 2007; Obara, 2002; Obara et al., 2004; Sugioka et al., 2012; To et al., 2015). These observations, together with the fact that the Nankai margin has been the focus of extensive geophysical imaging, geological, drilling, and geodetic campaigns, makes it an ideal natural laboratory to investigate subduction zone slip behavior and processes.

Extensive sample recovery from the Nankai Trough at depth via the (Integrated) Ocean Drilling Program ((I) ODP; e.g., Kimura et al., 2007) has allowed experimental characterization of the frictional properties of the shallow megathrust near the trench and its protolith (Bedford et al., 2021; Ikari & Kopf, 2017; Ikari & Saffer, 2011; Ikari et al., 2009; Kopf & Brown, 2003; Roesner et al., 2020; Takahashi et al., 2014; Tsutsumi et al., 2011; Ujiie & Tsutsumi, 2010). Of particular importance in the context of nucleating unstable slip are rate- and state friction (RSF) properties (Dieterich, 1979; Ruina, 1983). Here, we focus on the frictional stability parameters, which describe the response of friction to changes in driving velocity: for velocity-weakening, friction decreases with increased sliding rate, whereas it increases with slip velocity for velocity-strengthening behavior. Velocity-weakening friction is a prerequisite for the nucleation of unstable slip (Rice & Ruina, 1983).

Experiments performed at low slip velocities on materials sampled by drilling, aimed at addressing earthquake nucleation, suggest that frictional behavior becomes less stable with (a) increasing cohesion or lithification (Roesner et al., 2020), (b) decreasing clay content (Takahashi et al., 2014), (c) decreasing pore fluid pressures at constant effective normal stress (Bedford et al., 2021), and (d) decreasing slip velocity to plate velocities (Ikari & Kopf, 2017). All of these experiments were performed on materials derived from shallow levels (<1 km depth) and at temperatures <50°C (Takahashi et al., 2014), with most previous work at temperatures of ∼20°C–25°C— that is, much lower than the ∼100°C–350°C expected at seismogenic depths (Hyndman et al., 1997). Trütner et al. (2015) conducted room temperature experiments on samples exhumed from seismogenic depths (maximum paleo-temperatures of 125°C–225°C) and exposed in the Shimanto Belt in southwest Japan, and found an effect of composition and lithification as in (a). However, no experiments have been conducted at elevated temperatures on these materials.

Improved quantification of the frictional behavior of subduction megathrusts requires data from experiments performed at representative pressures and temperatures, and on samples having realistic compositions for fault rocks at seismogenic depths. Here, we quantify the in situ frictional behavior of metasediments from the Shimanto and Sanbagawa belts on Shikoku Island, southwest Japan, which have been exhumed from depths encompassing the seismogenic zone. We performed shearing experiments at the approximate in situ peak *PT* conditions for each sample, at different fluid overpressure ratios and at slip velocities relevant to earthquake nucleation. Our results are in agreement with previous findings by Den Hartog, Niemeijer, & Spiers (2012), who documented a control of temperature on frictional slip stability for subduction zone materials. In addition, our results show a consistent effect of slip velocity on frictional stability.

2. Materials and Methods

2.1. Sample Material

We used samples exhumed in the Shimanto Belt and Sanbagawa Belt on Shikoku Island, Japan (Figure 1). Peak paleo temperatures experienced by the samples were estimated from extensive previous work, including vitrinite reflectance and illite crystallinity studies (e.g., Awan & Imura, 1996; Laughland & Underwood, 1993; Ohmori et al., 1997) and are listed in Table S1 in Supporting Information S1. These samples were collected during a targeted field campaign (Trütner et al., 2015), and samples collected primarily from unweathered coastal or riverbed outcrop exposures of well-studied lithologies.
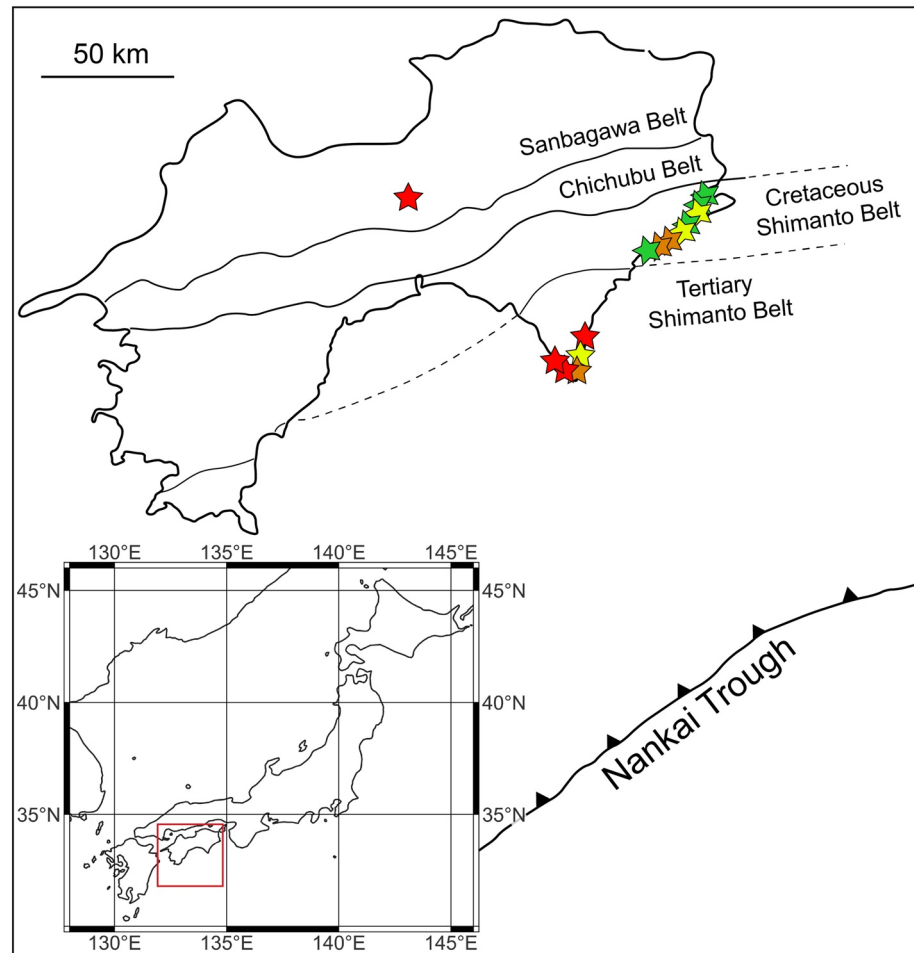
Figure 1. Map of Shikoku Island, southwest Japan showing the location of the samples used in this study with stars. Color represents the maximum in situ paleo temperature as follows: green = 100°C–150°C, yellow = 150°C–175°C, orange = 175°C–200°C, red = >200°C. Inset shows the location of Shikoku Island in Japan. For detailed geological maps of Shikoku Island, see Geological Survey of Japan (2022).

Samples were prepared by: (a) mechanically crushing to ∼0.5–1 cm, (b) crushing for ∼20 s in a disk mill, and (c) sieving to <106 μm. Steps (b) and (c) were repeated for materials not passing through the sieve to prevent sample fractionation. No information is available on grain sizes after sample preparation and how those compare to natural gouges. Ring-shaped samples of the gouges, measuring ∼1 mm in thickness and with inner and outer diameters of 22 and 28 mm, were prepared by pre-pressing mixtures of gouge and distilled water. Pressing was done at ∼170 MPa for 20 min at room temperature, using a specially designed die (Den Hartog, Peach, De Winter, Spiers, & Shimamoto, 2012).

X-Ray Diffraction analysis of the powdered samples (Table 1) by the method of Underwood et al. (2003) indicates that they comprise ∼50 wt% clay, 30 wt% quartz, and 20 wt% feldspar. The clay-sized (<2 μm) fraction was typically dominated by illite with smaller proportions of chlorite. These results indicate that all samples are pelites or metapelites. Although the bulk modal assemblages do not exhibit major systematic differences as a function of paleo-conditions, some differences are expected with prograde low-*T* metamorphism (e.g., abundance of amorphous Si cement, illite crystallinity; e.g., Trütner et al., 2015). Previous work (Den Hartog et al., 2021) suggests that even samples with similar compositions may show distinctly different frictional properties.

Table 1
Properties of Samples Used in This Study

Sample	Peak paleo temperature (°C)	Depth (km)	Composition bulk				Clay fraction			
			Clay	*Qtz*	*Fspar*	*Calc*	*Sm*	*Ill*	*Chl*	*Qtz*
DS-S2	112.5	7.8	51	29	20	0	0	62	32	7
DS-S4	200	13.9	55	25	20	0	0	70	21	9
DS-S6	105	7.4	45	24	31	0	0	72	15	13
DS-S8A	140	9.6	53	26	21	0	0	68	21	11
DS-S10	137.5	9.5	55	28	17	0	0	57	32	11
DS-S16	187.5	13.1	55	28	17	0	0	61	32	7
DS-S18	207.5	14.5	54	34	11	0	0	72	9	19
DS-S22	170	11.8	40	39	21	0	0	77	4	20
DS-S23	280	20.3	51	36	13	0	0	68	12	20
DS-S26	150	10.3	58	19	24	0	0	65	17	18
DS-S27	350	26.0	N.D.	N.D.	N.D.	N.D.	0	75	25	0
DS-S28	470	47.5	N.D.	N.D.	N.D.	N.D.	0	37	54	9

Note. Samples DS-S27 and DS-S28 were derived from the Sanbagawa Belt while all other samples were derived from the Shimanto Belt. The bulk composition of DS-S27 and DS-S28 could not be determined due to unmatched Singular Value Decomposition (SVD) factors. The XRD patterns of these two samples are shown in Figure S2 in Supporting Information S1. Depth is determined from the peak paleo temperature and the profiles in Spinelli and Wang (2009). Qtz = quartz, Fspar = feldspar, Calc = calcite, Sm = smectite, Ill = illite, Chl = chlorite.

2.2. Experimental Apparatus and Procedure

Rotary shear experiments were performed using a hydrothermal ring shear machine (Figure S1 in Supporting Information S1; Den Hartog, Niemeijer, et al., 2012; Den Hartog et al., 2013; Niemeijer et al., 2008). In this configuration, a ring-shaped sample with inner and outer radii of 11 and 14 mm is emplaced between two roughened pistons, located in an internally heated pressure vessel filled with distilled water, which applies a pore fluid pressure. To inhibit extrusion, the sample is confined between the loading pistons by steel rings. Normal stress is applied to the sample, in excess of the pore fluid pressure (P_f) measured in the vessel, via a pressure-compensated upper loading piston, so that the effective normal stress (σ_n^{eff}) is equal to the axially applied stress (Den Hartog, Niemeijer, et al., 2012). Rotation of the vessel and lower piston allow shearing of the sample at constant rate, while the shear stress (τ) is measured externally via the non-rotating upper piston. The experimental procedure we followed has been described by Den Hartog, Peach, et al. (2012). After a run-in at 10 μm/s for 5 mm of displacement, the slip velocity in the experiments was stepped between 0.1, 1, 10, and 100 μm/s, to assess frictional stability parameters. We report displacements and slip velocity at the average radius of the sample ring (12.5 mm); which varies by <14% over the sample width.

Shear displacement (resolution ±1 μm), axial displacement (±0.05 μm), normal force (±0.05 kN), and shear force (<±40 N or ±0.24 N depending on sensors used) were measured externally and the corresponding signals logged, together with the pore fluid pressure (±0.005 MPa) and temperature (±1°C) signals, using a 16 bit A/D converter and a logging frequency of 1–100 Hz (depending on the sliding velocity). Shear displacement was corrected for machine distortion, and torque and normal force data were corrected for seal friction to obtain the shear stress (τ) and effective normal stress acting on the sample, and the apparent friction coefficient ($\mu = \tau/\sigma_n^{eff}$, ignoring cohesion).

2.3. Experimental Conditions

Ring shear experiments were performed at the reported in situ peak *PT* conditions for each sample (Table 2), which range from 105°C to 470°C (Table 1). The expected in situ lithostatic pressure for each sample was estimated using modeled temperatures along the present-day Nankai subduction zone (Spinelli & Wang, 2009) and assuming an overburden density of 2,750 kg/m³. We set pore fluid pressure in our experiments to simulate values

Table 2
List of Experimental Conditions Used

Experiment	Material	T (°C)	σ_n^{eff} (MPa)		P_f (MPa)	λ		λ'	
RSDS-S2-1	DS-S2	112.5	73.89		137.2	0.65		0.65	
RSDS-S4-1	DS-S4	200	131.52		200	0.60		0.65	
RSDS-S6-1	DS-S6	105	69.43		128.9	0.65		0.65	
RSDS-S6-2	DS-S6	105	69.43		128.9	0.65		0.65	
RSDS-S6-3	DS-S6	105	69.43	85.96	128.9	0.65	0.60	0.65	0.57
			102.49	119.02		0.56	0.52	0.48	0.40
RSDS-S8A-1	DS-S8A	140	91.07		169.1	0.65		0.65	
RSDS-S10-1	DS-S10	137.5	89.52		166.3	0.65		0.65	
RSDS-S10-2	DS-S10	137.5	89.52		166.3	0.65		0.65	
RSDS-S16-1	DS-S16	187.5	123.29		229	0.65		0.65	
RSDS-S18-8	DS-S18	207.5	137.06		240	0.64		0.65	
RSDS-S18-9	DS-S18	207.5	39.16		200	0.84		0.90	
RSDS-S22-1	DS-S22	170	111.68		207.4	0.65		0.65	
RSDS-S23-1	DS-S23	280	191.50		240	0.56		0.65	
RSDS-S23-2	DS-S23	280	54.72		200	0.79		0.90	
RSDS-S26-1	DS-S26	150	97.52		181.1	0.65		0.65	
RSDS-S26-2	DS-S26	150	97.52		90	0.48		0.65	
RSDS-S26-3	DS-S26	150	97.52		200	0.67		0.65	
RSDS-S26-4	DS-S26	150	167.17		200	0.54		0.40	
RSDS-S26-5	DS-S26	150	27.86	47.79	200	0.88	0.81	0.90	0.83
			55.72			0.78		0.80	
RSDS-S26-6	DS-S26	150	55.72		200	0.78		0.80	
RSDS-S26-8	DS-S26	150	97.52		45	0.32		0.65	
RSDS-S27-1	DS-S27	350	70.26		200	0.74		0.90	
RSDS-S27-2	DS-S27	350	70.26		200	0.74		0.90	
RSDS-S27-3	DS-S27	350	70.26		200	0.74		0.90	
RSDS-S28-1	DS-S28	470	128.11		200	0.61		0.90	

Note. T, temperature, σ_n^{eff}, effective normal stress, P_f, pore fluid pressure, λ, fluid overpressure ratio, λ', modified fluid overpressure ratio.

of fluid overpressure ratio λ, defined as the ratio of pore fluid pressure to lithostatic pressure, equal to 0.65 or 0.90. However, machine limitations constrained our pore fluid pressure to 200 (or in some cases to 240 MPa). In cases where P_f was limited, we kept the effective normal stress σ_n^{eff}, at the level consistent with the target fluid overpressure ratio. The effective normal stress is defined as the difference between the normal stress, here equal to the lithostatic pressure, and the pore fluid pressure. The actual fluid overpressure ratio in experiments in which we could not reach the desired pore fluid pressure was therefore lower than the target value, but the effective stress was consistent with that expected in situ for the appropriate burial depth and target pore pressure ratio. We compare experiments according to their intended fluid overpressure ratio rather than the actual fluid overpressure ratio, and refer to the intended fluid overpressure ratio as λ' (Table 2). We used λ' values of 0.65 for 105°C–280°C and 0.90 for 150°C–470°C, due to limitations in the pore fluid pressure that could be generated.

2.4. Data Processing

The velocity dependence of friction was interpreted using the rate and state dependent friction (RSF) theory (Dieteric & Deiterich, 1978, 1979; Ruina, 1983), with the empirical Dieterich type ("slowness") formulation:

$$\mu = \mu_0 + a\ln\left(\frac{V}{V_0}\right) + b\ln\left(\frac{V_0\theta}{d_c}\right) \qquad \text{with} \qquad \frac{d_\theta}{dt} = 1 - \frac{V\theta}{d_c} \tag{1}$$

(e.g., Marone, 1998). Here, θ is an internal state variable, a represents the magnitude of the instantaneous change in μ upon a step change in sliding velocity from a value V_0 to a value $V = eV_0$, b reflects the magnitude of the change in μ during subsequent evolution to a new steady state value over a critical sliding distance d_c, and μ_0 is the friction coefficient measured at velocity V_0. For changes in steady state friction coefficient (μ_{ss}) resulting from a stepwise change in velocity, Equation 1 yields:

$$(a-b) = \frac{\Delta\mu_{ss}}{\Delta\ln V} \tag{2}$$

(e.g., Marone, 1998). Positive values of the rate parameter (a-b) indicate an increase in friction coefficient with increasing velocity (i.e., velocity-strengthening) while negative values indicate velocity-weakening (e.g., Scholz, 1998). Values of a, b, and d_c for our experiments were obtained using the RSFit3000 program by Skarbek and Savage (2019). This program is built around a nonlinear least squares fitting routine that uses the Levenberg-Marquardt method. In determining the RSF parameters, we applied detrending of the friction coefficient versus displacement curve to remove the effect of background slip hardening, following for example, Blanpied et al. (1998). Representative friction data from our experiments and model fits are shown in Figure S3 in Supporting Information S1.

3. Results

Some of our control experiments performed at identical conditions showed a variation in absolute values of friction coefficient (Figure S4 in Supporting Information S1) that could not be explained as experimental artifact. However, the RSF parameters of these control experiments were consistent (Figure S4 in Supporting Information S1). Therefore, in the following, we focus on RSF parameters. A Table of all RSF parameters is provided in Table S2 in Supporting Information S1.

3.1. Effect of Temperature, Pressure, and Effective Normal Stress on Frictional Properties

Sample paleo-depth is represented by temperature and effective normal stress. We show our data as a function of temperature, but the patterns observed are the same when RSF parameters are plotted as a function of effective normal stress (Figure S5 in Supporting Information S1).

Figure 2 shows the RSF parameters as a function of temperature for experiments performed at effective normal stresses corresponding to $\lambda' = 0.65$. Figures S6–S9 in Supporting Information S1 show the same data but with each velocity in a separate figure. No trends in any of the RSF parameters with temperature are apparent, and at all temperatures, behavior is velocity-strengthening to velocity-neutral or slightly velocity-weakening. Values of (a-b) (Figure 2a) vary between −0.011 at 105°C for a velocity step from 1 to 10 μm/s and 0.039 at 200°C for a velocity step from 10 to 100 μm/s. Overall, (a-b) values tend to be most positive for higher velocity (steps from 10 to 100 μm/s), which is driven by the combination of relatively high values of a (Figure 2b) and low values of b (Figure 2c). The critical slip distance d_c is <1 mm and does not show a temperature-dependence, but is generally larger for faster sliding velocities (10–100 μm/s) than lower velocities (0.1–1 μm/s). The RSF parameters up to 187.5°C are the same for experiments performed at $\lambda = 0.65$ and at $\lambda' = 0.65$; the RSF parameters at $\lambda = 0.65$ (i.e., for experiments where the target pore fluid pressure could be achieved) are shown in Figure S10 in Supporting Information S1 for completeness.

Figure 3 shows the RSF parameters as a function of temperature for experiments performed at effective stresses corresponding to $\lambda' = 0.90$. At these conditions, (a-b) values are mostly positive (velocity-strengthening behavior), except at 350°C, where 40% of the values are negative. Values range between −0.015 at 350°C for a velocity step from 10 to 100 μm/s and 0.030 at 150°C for a velocity step from 100 to 10 μm/s and show a rough decrease
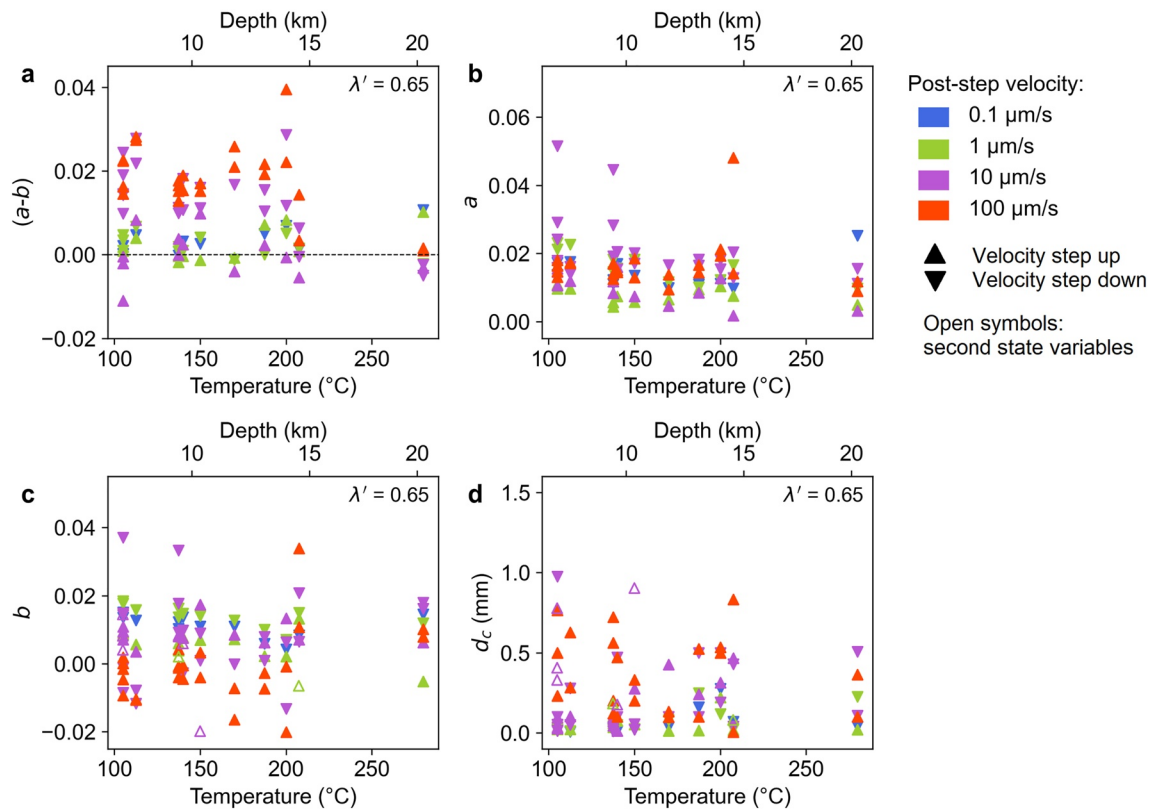
Figure 2. Rate- and state friction (RSF) parameters as a function of temperature and depth for experiments at $\lambda' = 0.65$. (a) values of $(a-b)$, (b) values of a, (c) values of b, and (d) values of d_c. Upward pointing triangles represent steps up in velocity, while downward pointing triangles denote steps down in velocity. Color-coding indicates post-step velocity. Open symbols in (c and d) represent second state variables.

with increasing temperature until 350°C, beyond which the values increase at 470°C. This pattern is primarily caused by decreasing values of a with increasing temperature until 350°C, followed by a slight increase between 350°C and 470°C. Although values of b are more randomly distributed with temperature, a very minor decrease of b with temperature can also be observed. The critical slip distance, like at $\lambda' = 0.65$, is typically <1 mm and shows a very weak increase with temperature.

Figure 4 shows values of the RSF parameter $(a-b)$ versus effective normal stress (Figure 4a) and pore fluid pressure (Figure 4b) at 150°C. At all conditions tested, $(a-b)$ values are positive to slightly negative. At low effective normal stresses and high pore fluid pressure, the spread in $(a-b)$ values is larger, in particular reaching larger positive values than at high effective normal stress or low pore fluid pressure, respectively. The (actual) fluid overpressure ratio λ is shown at the top axis in Figure 4b. Our data indicate a slight decrease of $(a-b)$ with effective stress, corresponding to a slight increase with λ.

3.2. Effect of Slip Velocity on Frictional Properties

Figures 5a and 6a show values of frictional rate dependence $(a-b)$ as a function of slip velocity for effective stresses corresponding to $\lambda' = 0.65$ and $\lambda' = 0.90$, respectively. There appears to be a positive trend of $(a-b)$ with increasing post-step slip velocity at lower temperatures, while data at higher T shows no or a slight negative trend with increasing post-step slip velocity (see also Figures S11–S22 in Supporting Information S1). In particular, at $\lambda' = 0.65$, data for experiments performed at 105°C–200°C show an increase in $(a-b)$ with increasing post-step slip velocity, while the experiment performed at 207.5°C shows a near-constant $(a-b)$ value and the experiment at 280°C shows a neutral to negative trend of $(a-b)$ with post-step slip velocity. Inspection of trends in a and b (Figures 5b and 5c) show that the positive trend at temperatures up to 200°C are caused by an increase in a and decrease in b with post-step slip velocity. Exceptions are some of the data for velocity downsteps at 105°C, which show a more significant increase in a with post-step slip velocity and only a minor decrease or even increase in
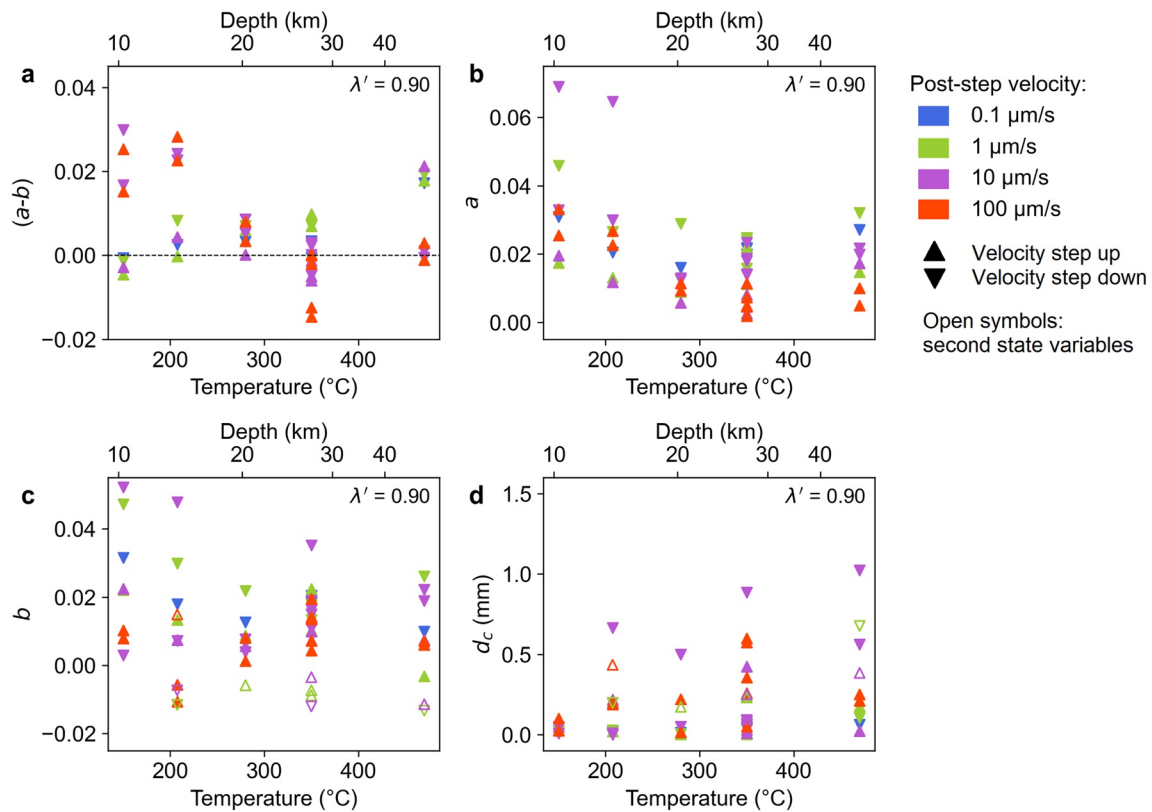
Figure 3. Rate- and state friction (RSF) parameters as a function of temperature and depth for experiments at $\lambda' = 0.90$. (a) values of $(a\text{-}b)$, (b) values of a, (c) values of b, and (d) values of d_c. Upward pointing triangles represent steps up in velocity, while downward pointing triangles denote steps down in velocity. Color-coding indicates post-step velocity. Open symbols in (c and d) represent second state variables.

b, still resulting in an increase in $(a\text{-}b)$ with increasing post-step slip velocity. At 207.5°C, both a and b increase with post-step slip velocity, resulting in values of $(a\text{-}b)$ that are constant with post-step slip velocity. Finally, at 280°C, no clear trends can be recognized in a and b with post-step slip velocity, resulting in neutral to slightly negative $(a\text{-}b)$ values with post-step slip velocity. A weak increase of d_c with post-step slip velocity seems to be present for velocity downsteps (Figure 5d).

At effective stresses corresponding to $\lambda' = 0.90$, the experiments performed at 150°C and 207.5°C show positive trends of $(a\text{-}b)$ with increasing post-step slip velocity, while the experiment performed at 280°C shows a
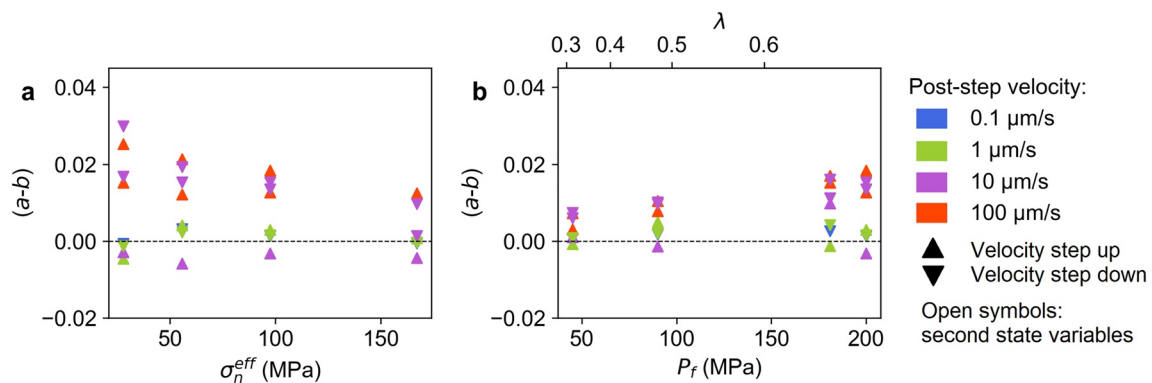

Figure 4. Rate- and state friction (RSF) parameter $(a\text{-}b)$ as a function of effective normal stress (a) and pore fluid pressure (b) at 150°C. All experiments in (a) are performed at a pore fluid pressure of 200 MPa, while all experiments in (b) are performed at an effective normal stress of 97.5 MPa. Upward pointing triangles represent steps up in velocity, while downward pointing triangles denote steps down in velocity. Color-coding indicates post-step velocity. The fluid overpressure ratio is shown at the top x-axis in (b).
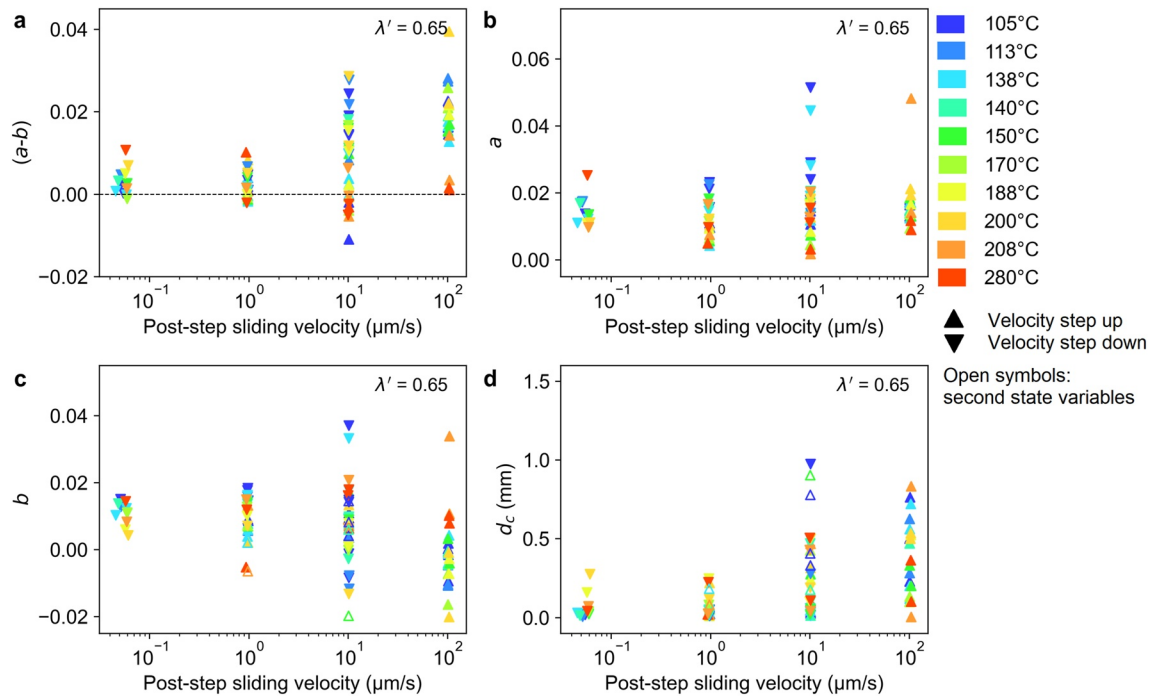
Figure 5. Rate- and state friction (RSF) parameters as a function of post-step sliding velocity for $\lambda' = 0.65$. (a) values of $(a-b)$, (b) values of a, (c) values of b and (d) values of d_c. Upward pointing triangles represent steps up in velocity, while downward pointing triangles denote steps down in velocity. Color-coding indicates temperature where the colors change from blue to green, to yellow to red with increasing temperature. Open symbols in (c and d) represent second state variables.
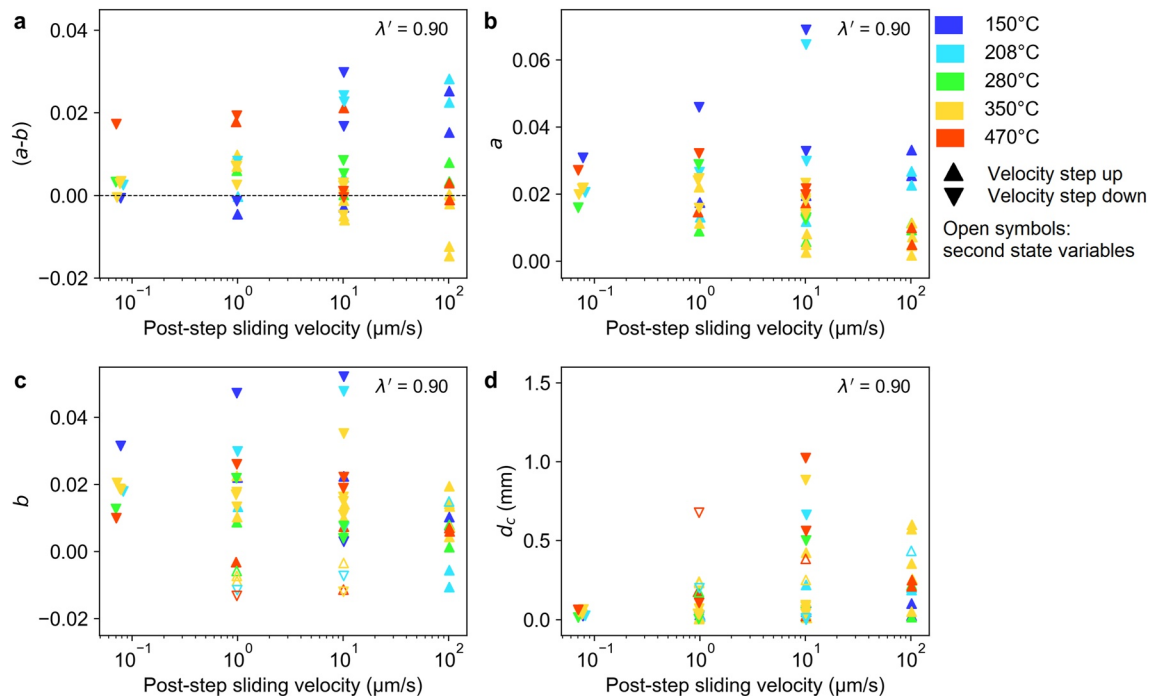

Figure 6. Rate- and state friction (RSF) parameters as a function of post-step sliding velocity for $\lambda' = 0.90$. (a) values of $(a-b)$, (b) values of a, (c) values of b and (d) values of d_c. Upward pointing triangles represent steps up in velocity, while downward pointing triangles denote steps down in velocity. Color-coding indicates temperature where the colors change from blue to green, to orange to red with increasing temperature. Open symbols in (c and d) represent second state variables.

near-constant value of (*a-b*) and the experiment performed at 350°C a slight negative trend in (*a-b*) with increasing post-step slip velocity (Figure 6a). Finally, the experiment performed at 470°C shows a change from relatively large positive (*a-b*) values at post-step velocities of 1 and 10 μm/s (velocity upsteps) and 0.1 and 1 μm/s (velocity downsteps) to near-neutral (*a-b*) values at the highest post-step velocity (100 and 10 μm/s for velocity upsteps and downsteps, respectively). Trends in *a* and *b* (Figures 6b and 6c) show that the positive trends in (*a-b*) with increasing post-step slip velocity at 150°C and 207.5°C are due to either a relatively large increase in *a* combined with a smaller increase in *b*, or relatively constant values of *a* combined with a decrease in *b*. At higher temperatures, both *a* and *b* decrease with increasing post-step sliding velocity, where a somewhat larger decrease in *a* causes slightly negative values at high post-step velocities. Finally, values of d_c (Figure 6d) tend to be larger at higher post-step sliding velocities.

4. Discussion

4.1. Dependence of Frictional Properties on Temperature, Stress, and Velocity

Our results suggest that the most important variable affecting megathrust frictional properties is temperature, consistent with the general interpretation of seismicity along subduction zones (Hyndman et al., 1997). We observe a direct relationship between (*a-b*) and temperature at effective stresses corresponding to *λ'* = 0.90, yielding the most negative (*a-b*) values at an intermediate temperature of 350°C. In addition, our data show clear temperature-dependent trends of (*a-b*) with sliding velocity (cf. Figure 6). Notably, a positive trend of (*a-b*) with increasing slip velocity exists at temperatures up to 200°C–207.5°C, while data at higher temperatures show no or a slight negative trend with increasing velocity (Figures 5 and 6).

A number of studies have addressed the effect of temperature on fault frictional properties, in the context of subduction megathrusts (Boulton et al., 2019; Den Hartog, Niemeijer, et al., 2012; Ikari et al., 2013) and continental faults (e.g., Niemeijer et al., 2016; Valdez et al., 2019). These studies have shown that under subduction zone conditions carbonates may cause velocity-weakening behavior (Boulton et al., 2019; Ikari et al., 2013) at temperatures up to 225°C. Carbonate-free, clay-rich gouges showed a transition from velocity-strengthening to velocity-weakening at 150°C–180°C for gouges from the Alpine Fault, New Zealand (Niemeijer et al., 2016; Valdez et al., 2019) or ~250°C for simulated megathrust gouges (Den Hartog, Niemeijer, et al., 2012). A transition back to velocity-strengthening behavior at a temperature of around 400°C was observed under some conditions (Den Hartog, Niemeijer, et al., 2012; Niemeijer et al., 2016), which is consistent with our data (Figure 3).

The effect of sliding velocity on RSF parameters for megathrust fault materials has also been reported in a number of studies (e.g., Ikari & Kopf, 2017; Rabinowitz et al., 2018; Saffer & Wallace, 2015; Shreedharan et al., 2022). In particular, these studies found a transition from near-neutral or slightly negative (*a-b*) values at low slip velocities to positive (*a-b*) values at higher slip velocities for materials relevant for subduction megathrusts, but have generally explored a limited set of (mostly low; <100°C) temperature conditions. The reported transition from velocity weakening to strengthening in clay-rich gouges generally occurs at velocities of ~0.1–1 μm/s (Ikari & Kopf, 2017; Shreedharan et al., 2022), consistent with our data for temperatures of 207.5°C and lower (Figures 5 and 6). None of these previous studies reported the systematic effect of temperature on the evolution of (*a-b*) with sliding velocity. In contrast, Niemeijer et al. (2016) found effects of both temperature and slip velocity on (*a-b*) for materials from the Alpine Fault. Importantly, the most positive (*a-b*) values were found at temperatures below about 200°C and sliding velocities above ~10 μm/s, while the most negative (*a-b*) values were found at ~300°C and velocities of ~1–0.1 μm/s. Although we conducted experiments on different materials at different effective normal stresses and pore fluid pressures, the conditions for the most positive (*a-b*) values are very similar to these previous studies (Figures 5 and 6). The neutral to negative trends in (*a-b*) at temperatures above about 207.5°C show some agreement with the results of Niemeijer et al. (2016).

Our data show some systematic variation in the RSF parameters *a*, *b*, and d_c. Although most trends are weak, at effective stresses corresponding to *λ'* = 0.90, both *a* and *b* decrease with increasing temperature, followed by an increase from 350°C to 470°C for *a*. We further observe an increase in d_c with temperature. Previous studies have found various trends of the RSF parameters with temperature. For example, Valdez et al. (2019) observed no clear trend in *a* with temperature, while *b* increased with temperature. Boulton et al. (2019), in contrast, found for clay-rich sediments from the Hikurangi subduction zone a minor increase in *a* with temperature and a decrease in *b*. Overall, our data are most consistent with that of Boulton et al. (2019). The increase in d_c we observe with

increasing temperature is consistent with that reported by Valdez et al. (2019), though our maximum d_c values are larger (1.5 vs. ~0.47 mm). With increasing slip velocity, the clearest trends in our data are, for a, (a) an increase with slip velocity up to 200°C at $λ' = 0.65$, and (b) a decrease with slip velocity at temperatures from 207.5°C at $λ' = 0.90$. For b, the main trends are (c) a decrease with slip velocity at temperature up to 200°C and $λ' = 0.65$, and (d) an increase with slip velocity at temperatures from 207.5°C. For d_c, we observe a small increase with slip velocity at both fluid overpressure ratios explored. Boulton et al. (2019) found positive trends of both a and b with sliding velocity for their clay-rich sediments at temperatures up to 225°C and a fluid overpressure ratio of 0.4, which is in agreement with our trend in a, but not that in b.

XRD analysis of our samples showed no systematic differences in sample composition as a function of paleo-conditions and thus our results do not allow for distinguishing the effect of composition on frictional slip stability. However, recent results by Den Hartog et al. (2021) suggest that even samples with similar bulk compositions may show distinctly different frictional properties. This was hypothesized to be caused by the presence and distribution of the clay mineral kaolinite and it may also relate to fabric development (e.g., Collettini et al., 2009). Our experiments do not allow for determining any similar effect of other clay minerals, as conditions were varied per sample.

In addition, our data suggest a small effect of effective stress (or $λ'$) on (a-b), at least at 150°C and 207.5°C (Figure 4b). This is consistent with Bedford et al. (2021), who found an increase in (a-b) with increasing pore fluid pressures at constant normal stress for Nankai gouges.

Finally, as explained in the Results section, we observed variation in absolute values of friction coefficient for some of our control experiments performed at identical conditions. We, therefore, do not provide a detailed comparison of the absolute values of the friction coefficient with literature data. Note that such a comparison would need to take into account factors such as shear displacement and temperature, which have been shown to affect the absolute value of friction coefficient (e.g., Den Hartog, Niemeijer, et al., 2012).

4.2. Deformation Mechanisms

No microstructural images were obtained in the current study and we, therefore, compare our data with the literature to speculate on possible deformation mechanisms. The velocity-weakening behavior at 350°C and predominantly velocity-strengthening behavior at lower and higher temperatures, most evident in our experiments at stresses corresponding to $λ' = 0.90$ is consistent with data for phyllosilicate-quartz gouge by Den Hartog, Niemeijer, et al. (2012). The possible microphysical processes are schematically shown in Figure 7 (Den Hartog & Spiers, 2014; see also Bos & Spiers, 2002; J. Chen & Spiers, 2016; Niemeijer & Spiers, 2007). At 200°C–300°C, slip on horizontal phyllosilicate foliation at critical state porosities causes velocity-strengthening (cf. Den Hartog et al., 2020). At 300°C–400°C, slip on phyllosilicates anastomosing around intervening clasts leads to dilation, balanced at steady state by compaction through thermally activated clast deformation, resulting in velocity-weakening. At temperatures of 400°C–500°C, slip on phyllosilicate foliation and thermally activated deformation of clasts lead to velocity-strengthening behavior.

The model proposed by Den Hartog and Spiers (2014) is applicable to matrix-supported gouges with 39%–79% quartz clasts and assumes pressure solution as the key thermally activated mechanism. Although our gouges contain feldspar as well as quartz clasts, both minerals show increasing dissolution with increasing temperature (e.g., Y. Chen & Brantley, 1997; Rimstidt & Barnes, 1980), suggesting that similar deformation mechanisms as proposed in this model might be applicable. Note that crystal plasticity as a thermally activated mechanism would produce similar slip stability trends as pressure solution. Though rates of crystal plasticity are likely too low at the conditions used (cf. Den Hartog, Niemeijer, et al., 2012), microstructural investigations would be needed to distinguish crystal plasticity from pressure solution.

The model of Den Hartog and Spiers (2014) does not make predictions for the evolution of individual RSF parameters. J. Chen et al. (2017) and J. Chen and Spiers (2016), however, developed a microphysical model that is very similar except that slip on phyllosilicates is not included, and made predictions of the evolution of a, b, and d_c. J. Chen et al. (2017) and J. Chen and Spiers (2016) explain a as the positive rate dependence of grain boundary friction and show that it is proportional to the temperature and inversely proportional to the normal stress supported by individual asperities. With increasing depth, their model predicts an increase in a followed by a decrease with increasing temperature and finally an increase when flow processes become dominant. The
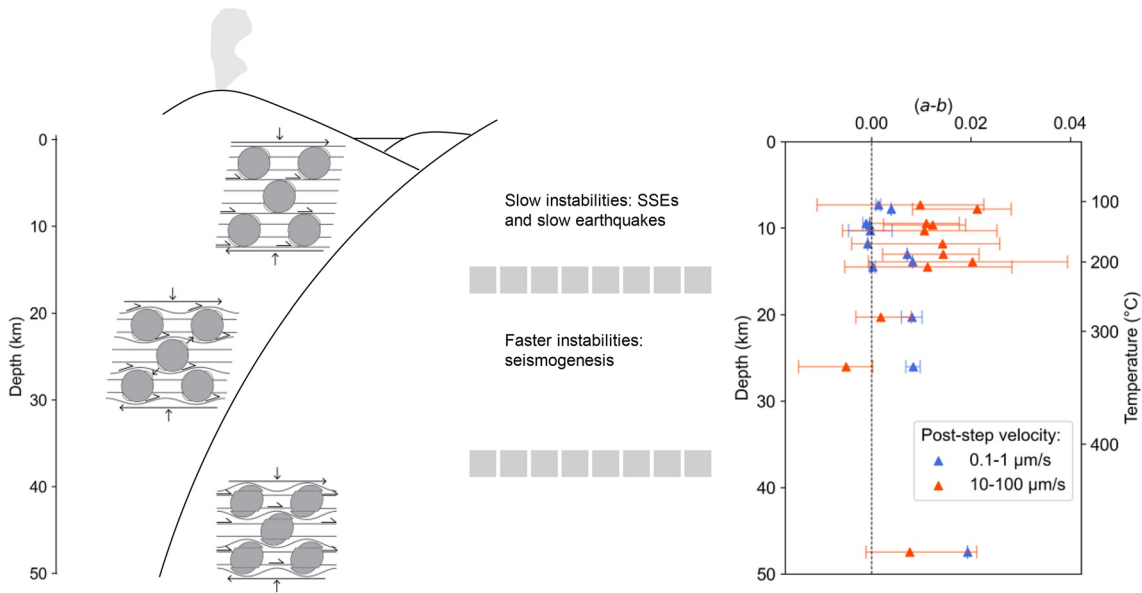
Figure 7. Summary of our data and implication for subduction zone seismogenesis—see text for explanation. Schematic cross-section of subduction zone is after Scholz (1998) and is horizontally compressed. Insets show the proposed microphysical processes as a function of depth after Den Hartog and Spiers (2014; see also Section 4.2) where clasts are shown in gray and phyllosilicate foliation as lines. Mean values of (*a-b*) at each depth are shown. Only velocity upsteps are considered for (*a-b*) as those are most relevant for slip nucleation.

decrease of *a* with temperature that we observed at temperature up to 350°C is consistent with this. A nearly constant value of *a* with slip velocity is predicted by J. Chen et al. (2017), which may explain why we observed both an increase and decrease of *a* with slip velocity. J. Chen et al. (2017) argue that processes such as grain size reduction, cohesion and (de)localization may also result in variations of *a* with slip velocity.

Previous works have interpreted d_c as the critical slip distance associated with the evolution of the porosity in response to small perturbations (e.g., Segall & Rice, 1995). A positive dependence of d_c on slip rate is also observed by Mair and Marone (1999) for granular quartz gouge, which is consistent with our finding of a weak increase of d_c with increasing slip velocity. In addition, previous works have suggested that d_c is proportional to the thickness of the shear zone and slip localization (J. Chen et al., 2017; Marone et al., 2009). Such a decrease in d_c with shear localization was also observed by Marone et al. (1993) and Kilgore. We did not observe any systematic change of d_c with strain, suggesting that localization effects in our experiments were minor, or that the shear localized in multiple shear bands throughout the entire experiment (cf. Den Hartog & Spiers, 2014). Finally, we note that lithification and consequently destabilization of slip (e.g., Saffer & Marone, 2003; Trütner et al., 2015) is unlikely in our experiments given the experimental duration on the order of hours.

4.3. Implications for Megathrust Seismogenesis

The temperature-dependent rate dependence of (*a-b*) that we observe for samples exhumed from the Nankai megathrust has implications for megathrust seismogenesis. Our data and interpretation are summarized in Figure 7. We propose that at low temperatures, below about 200°C–210°C, the increase in (*a-b*) with slip velocity implies that any instability that nucleates will stabilize during acceleration. As a consequence, slow instability or stable slip is favored at low temperatures, resulting in either aseismic creep or slow slip events (SSE) and slow earthquakes. The generation of SSE as a result of a transition from rate-weakening slip at low slip rates to rate-neutral or rate-strengthening behavior at higher slip rates has been proposed on the basis of experimental data at low temperature (e.g., Rabinowitz et al., 2018; Saffer & Wallace, 2015) and demonstrated via numerical simulations (e.g., Im et al., 2020; Shibazaki & Shimamoto, 2007). At higher temperatures, above about 200°C–210°C, the decrease of (*a-b*) with slip velocity observed in our experiments suggests that any instabilities that nucleate under these conditions will become increasingly unstable with increasing displacement rates. Thus, at high temperatures, we expect instabilities that may show runaway slip behavior and thus result in seismogenesis. This distinction between shallow, slow instabilities and deeper seismogenesis is consistent with the general

range of behaviors observed at subduction zones (e.g., Bilek & Lay, 2018). At the highest temperature of 470°C explored here, larger positive (*a-b*) values are obtained at lower slip velocities, consistent with the location of a downdip limit to the seismogenic zone.

Based on experimental observations, elevated pore-fluid pressures at patches in a subduction zone setting have been put forward by Bedford et al. (2021) as an alternative to displacement rate to cause a transition from velocity-weakening to velocity-strengthening behavior, inducing slow slip behavior or aseismic creep. In their experiments, the transition was related to increasingly negative values of *b* at high pore fluid pressures. The experimental data of these authors could not confirm their hypothesis, as only velocity-strengthening behavior was observed. Although our data suggest a possible minor increase in (*a-b*) with λ (Figure 4), which would be consistent with the hypothesis of Bedford et al. (2021), more data is needed for a convincing argument; instead, our available data shows a clear effect of slip velocity and temperature.

Finally, we note that our results are most relevant to subduction zones where clay-rich hemipelagic sediments are entrained along and form the protolith for the plate boundary. Our work – along with that done for the Alpine Fault - suggests that similar systematic investigations of frictional behavior for carbonate-rich megathrusts would yield valuable insight into subduction zone seismogenesis.

5. Conclusions

We measured the frictional behavior of sediments and metasediments representing relevant analogs for fault materials along the Nankai Trough subduction megathrust at depths encompassing the seismogenic zone. These materials include rocks exhumed in the Shimanto Belt and Sanbagawa Belt on Shikoku Island, and which we sheared at the sample-specific, approximate in situ peak *PT* conditions at different fluid overpressure ratios and low slip velocities to address earthquake nucleation. Our results show predominantly velocity-strengthening behavior; velocity-weakening behavior was observed at 350°C with velocity-strengthening behavior at lower and higher temperatures. A notable effect of slip velocity on (*a-b*) was observed in our data, being predominantly positive at temperatures up to 200°C–210°C and neutral or negative at higher temperatures. Our experimental data are consistent with previous experimental work on fault rocks over a range of *P-T* conditions, and the observed trends in frictional stability with temperature, normal stress, and sliding velocity can be explained, to first order, by microphysical models that describe a competition between pressure solution and dilatancy (e.g., J. Chen et al., 2017; Den Hartog, Niemeijer, et al., 2012). We propose that this temperature- and rate-dependent rate dependence of friction may explain the predominance of slow instabilities such as slow slip events at shallow depths, and faster instabilities and seismogenesis at greater depths.

Data Availability Statement

The experimental data presented in this manuscript can be found in Den Hartog et al. (2019).

References

Ando, M. (1975). Source mechanisms and tectonic significance of historical earthquakes along the Nankai Trough, Japan. *Tectonophysics*, *27*(2), 119–140. https://doi.org/10.1016/0040-1951(75)90102-X

Araki, E., Saffer, D. M., Kopf, A. J., Wallace, L. M., Kimura, T., Machida, Y., et al. (2017). Recurring and triggered slow-slip events near the trench at the Nankai Trough subduction megathrust. *Science*, *356*(6343), 1157–1160. https://doi.org/10.1126/science.aan3120

Awan, M. A., & Imura, K. (1996). Thermal structure and uplift of the Cretaceous Shimanto Belt, Kii Peninsula, southwest Japan: An illite crystallinity and Mite b_o, lattice spacing study. *Island Arc*, *5*(1), 69–88. https://doi.org/10.1111/j.1440-1738.1996.tb00013.x

Bedford, J. D., Faulkner, D. R., Allen, M. J., & Hirose, T. (2021). The stabilizing effect of high pore-fluid pressure along subduction megathrust faults: Evidence from friction experiments on accretionary sediments from the Nankai Trough. *Earth and Planetary Science Letters*, *574*, 117161. https://doi.org/10.1016/j.epsl.2021.117161

Bilek, S. L., & Lay, T. (2018). Subduction zone megathrust earthquakes. *Geosphere*, *14*(4), 1468–1500. https://doi.org/10.1130/ges01608.1

Blanpied, M. L., Marone, C. J., Lockner, D. A., Byerlee, J. D., & King, D. P. (1998). Quantitative measure of the variation in fault rheology due to fluid-rock interactions. *Journal of Geophysical Research*, *103*(B5), 9691–9712. https://doi.org/10.1029/98jb00162

Bos, B., & Spiers, C. J. (2002). Frictional-viscous flow of phyllosilicate-bearing fault rock: Microphysical model and implications for crustal strength profiles. *Journal of Geophysical Research*, *107*(B2). https://doi.org/10.1029/2001JB000301

Boulton, C., Niemeijer, A. R., Hollis, C. J., Townend, J., Raven, M. D., Kulhanek, D. K., & Shepherd, C. L. (2019). Temperature-dependent frictional properties of heterogeneous Hikurangi Subduction Zone input sediments, ODP Site 1124. *Tectonophysics*, *757*, 123–139. https://doi.org/10.1016/j.tecto.2019.02.006

Chen, J., Niemeijer, A. R., & Spiers, C. J. (2017). Microphysically derived expressions for rate-and-state friction parameters, *a*, *b*, and d_c. *Journal of Geophysical Research: Solid Earth*, *122*(12), 9627–9657. https://doi.org/10.1002/2017JB014226

Chen, J., & Spiers, C. J. (2016). Rate and state frictional and healing behavior of carbonate fault gouge explained using microphysical model. *Journal of Geophysical Research: Solid Earth*, *121*(12), 8642–8665. https://doi.org/10.1002/2016JB013470

Chen, Y., & Brantley, S. L. (1997). Temperature- and pH-dependence of albite dissolution rate at acid pH. *Chemical Geology*, *135*(3), 275–290. https://doi.org/10.1016/S0009-2541(96)00126-X

Collettini, C., Niemeijer, A., Viti, C., & Marone, C. (2009). Fault zone fabric and fault weakness. *Nature*, *462*(7275), 907–910. https://doi.org/10.1038/nature08585

Cowan, D. S. (1999). Do faults preserve a record of seismic slip? A field geologist's opinion. *Journal of Structural Geology*, *21*(8–9), 995–1001. https://doi.org/10.1016/s0191-8141(99)00046-2

Den Hartog, S. A. M., Faulkner, D. R., & Spiers, C. J. (2020). Low friction coefficient of phyllosilicate fault gouges and the effect of humidity: Insights from a new microphysical model. *Journal of Geophysical Research: Solid Earth*, *125*(6), e2019JB018683. https://doi.org/10.1029/2019jb018683

Den Hartog, S. A. M., Niemeijer, A. R., & Spiers, C. J. (2012). New constraints on megathrust slip stability under subduction zone *P-T* conditions. *Earth and Planetary Science Letters*, *353–354*, 240–252. https://doi.org/10.1016/j.epsl.2012.08.022

Den Hartog, S. A. M., Niemeijer, A. R., & Spiers, C. J. (2013). Friction on subduction megathrust faults: Beyond the illite-muscovite transition. *Earth and Planetary Science Letters*, *373*, 8–19. https://doi.org/10.1016/j.epsl.2013.04.036

Den Hartog, S. A. M., Peach, C. J., De Winter, D. A. M., Spiers, C. J., & Shimamoto, T. (2012). Frictional properties of megathrust fault gouges at low sliding velocities: New data on effects of normal stress and temperature. *Journal of Structural Geology*, *38*, 156–171. https://doi.org/10.1016/j.jsg.2011.12.001

Den Hartog, S. A. M., Saffer, D. M., Marone, C. J., & Niemeijer, A. R. (2019). Frictional properties of megathrust gouges [Dataset]. Interdisciplinary Earth Data Alliance (IEDA). https://doi.org/10.1594/IEDA/100669

Den Hartog, S. A. M., Saffer, D. M., & Spiers, C. J. (2014). The roles of quartz and water in controlling unstable slip in phyllosilicate-rich megathrust fault gouges. *Earth Planets and Space*, *66*(78). https://doi.org/10.1186/1880-5981-66-78

Den Hartog, S. A. M., & Spiers, C. J. (2014). A microphysical model for fault gouge friction applied to subduction megathrusts. *Journal of Geophysical Research: Solid Earth*, *119*(2), 1510–1529. https://doi.org/10.1002/2013jb010580

Den Hartog, S. A. M., Thomas, M. Y., & Faulkner, D. R. (2021). How do laboratory friction parameters compare with observed fault slip and geodetically derived friction parameters? Insights from the longitudinal valley fault, Taiwan. *Journal of Geophysical Research: Solid Earth*, *126*(10), e2021JB022390. https://doi.org/10.1029/2021JB022390

Dieterich, J. H. (1978). Time-dependent friction and the mechanics of stick-slip. *Pure and Applied Geophysics*, *116*(4–5), 790–806. https://doi.org/10.1007/bf00876539

Dieterich, J. H. (1979). Modeling of rock friction 1. Experimental results and constitutive equations. *Journal of Geophysical Research*, *84*(B5), 2161–2168.

Geological Survey of Japan. (2022). Retrieved from https://www.gsj.jp/Map/EN/geology2-5.html

Hirose, H., & Obara, K. (2005). Repeating short- and long-term slow slip events with deep tremor activity around the Bungo channel region, southwest Japan. *Earth Planets and Space*, *57*(10), 961–972. https://doi.org/10.1186/bf03351875

Hyndman, R. D., Yamano, M., & Oleskevich, D. A. (1997). The seismogenic zone of subduction thrust faults. *Island Arc*, *6*(3), 244–260. https://doi.org/10.1111/j.1440-1738.1997.tb00175.x

Iio, Y., Kobayashi, Y., & Tada, T. (2002). Large earthquakes initiate by the acceleration of slips on the downward extensions of seismogenic faults. *Earth and Planetary Science Letters*, *202*(2), 337–343. https://doi.org/10.1016/s0012-821x(02)00776-8

Ikari, M. J., & Kopf, A. J. (2017). Seismic potential of weak, near-surface faults revealed at plate tectonic slip rates. *Science Advances*, *3*(11), e1701269. https://doi.org/10.1126/sciadv.1701269

Ikari, M. J., Niemeijer, A. R., Spiers, C. J., Kopf, A. J., & Saffer, D. M. (2013). Experimental evidence linking slip instability with seafloor lithology and topography at the Costa Rica convergent margin. *Geology*, *41*(8), 891–894. https://doi.org/10.1130/g33956.1

Ikari, M. J., & Saffer, D. M. (2011). Comparison of frictional strength and velocity dependence between fault zones in the Nankai accretionary complex. *Geochemistry, Geophysics, Geosystems*, *12*(4), Q0AD11. https://doi.org/10.1029/2010gc003442

Ikari, M. J., Saffer, D. M., & Marone, C. (2009). Frictional and hydrologic properties of a major splay fault system, Nankai subduction zone. *Geophysical Research Letters*, *36*(20), L20313. https://doi.org/10.1029/2009gl040009

Im, K., Saffer, D., Marone, C., & Avouac, J.-P. (2020). Slip-rate-dependent friction as a universal mechanism for slow slip events. *Nature Geoscience*, *13*(10), 705–710. https://doi.org/10.1038/s41561-020-0627-9

Ito, Y., Hino, R., Kido, M., Fujimoto, H., Osada, Y., Inazu, D., et al. (2013). Episodic slow slip events in the Japan subduction zone before the 2011 Tohoku-Oki earthquake. *Tectonophysics*, *600*, 14–26. https://doi.org/10.1016/j.tecto.2012.08.022

Ito, Y., Obara, K., Shiomi, K., Sekine, S., & Hirose, H. (2007). Slow earthquakes coincident with episodic tremors and slow slip events. *Science*, *315*(5811), 503–506. https://doi.org/10.1126/science.1134454

Kano, M., Kato, A., & Obara, K. (2019). Episodic tremor and slip silently invades strongly locked megathrust in the Nankai Trough. *Scientific Reports*, *9*(1), 9270. https://doi.org/10.1038/s41598-019-45781-0

Kimura, G., Screaton, E. J., & Curewitz, D. (2007). NanTroSEIZE Stage 1: NanTroSEIZE shallow megasplay and frontal thrusts. *IODP Scientific Prospectus*, *316*. https://doi.org/10.2204/iodp.sp.2316.2007

Kopf, A., & Brown, K. M. (2003). Friction experiments on saturated sediments and their implications for the stress state of the Nankai and Barbados subduction thrusts. *Marine Geology*, *202*(3), 193–210. https://doi.org/10.1016/S0025-3227(03)00286-X

Laughland, M. M., & Underwood, M. B. (1993). Vitrinite reflectance and estimates of paleo temperature within the upper Shimanto Group, Muroto Peninsula, Shikoku, Japan. https://doi.org/10.1016/S0025-3227(03)00286-X

Lay, T. (2018). A review of the rupture characteristics of the 2011 Tohoku-oki Mw 9.1 earthquake. *Tectonophysics*, *733*, 4–36. https://doi.org/10.1016/j.tecto.2017.09.022

Lay, T., & Bilek, S. L. (2007). Anamalous earthquake ruptures at shallow depths on subduction zone megathrusts. In T. H. Dixon, & J. C. Moore (Eds.), *The seismogenic zone of subduction thrust faults* (pp. 476–511). Columbia University Press.

Liu, Y., & Rice, J. R. (2005). Aseismic slip transients emerge spontaneously in three-dimensional rate and state modeling of subduction earthquake sequences. *Journal of Geophysical Research*, *110*(B8), B08307. https://doi.org/10.1029/2004JB003424

Mair, K., & Marone, C. (1999). Friction of simulated fault gouge for a wide range of velocities and normal stresses. *Journal of Geophysical Research: Solid Earth*, *104*(B12), 28899–28914. https://doi.org/10.1029/1999jb900279

Marone, C. (1998). Laboratory-derived friction laws and their application to seismic faulting. *Annual Review of Earth and Planetary Sciences*, *26*(1), 643–696. https://doi.org/10.1146/annurev.earth.26.1.643

Marone, C., Cocco, M., Richardson, E., & Tinti, E. (2009). The critical slip distance for seismic and aseismic fault zones of finite width. In E. Fukuyama (Ed.), *Fault-zone properties and earthquake rupture dynamics*, *International Geophysics Series* (Vol. 94, pp. 135–162). Elsevier.

Marone, C., & Kilgore, B. (1993). Scaling of the critical slip distance for seismic faulting with shear strain in fault zones. *Nature*, *362*(6421), 618–621. https://doi.org/10.1038/362618a0

Moore, J. C., & Saffer, D. (2001). Updip limit of the seismogenic zone beneath the accretionary prism of southwest Japan: An effect of diagenetic to low-grade metamorphic processes and increasing effective stress. *Geology*, *29*(2), 183–186. https://doi.org/10.1130/0091-7613(2001)029<0183:ULOTSZ>2.0.CO;2

Niemeijer, A. R., Boulton, C., Toy, V. G., Townend, J., & Sutherland, R. (2016). Large-displacement, hydrothermal frictional properties of DFDP-1 fault rocks, Alpine Fault, New Zealand: Implications for deep rupture propagation. *Journal of Geophysical Research: Solid Earth*, *121*(2), 624–647. https://doi.org/10.1002/2015jb012593

Niemeijer, A. R., & Spiers, C. J. (2007). A microphysical model for strong velocity weakening in phyllosilicate-bearing fault gouges. *Journal of Geophysical Research*, *112*(B10405), B10405. https://doi.org/10.1029/2007JB005008

Niemeijer, A. R., Spiers, C. J., & Peach, C. J. (2008). Frictional behavior of simulated quartz fault gouges under hydrothermal conditions: Results from ultra-high strain rotary shear experiments. *Tectonophysics*, *460*(1–4), 288–303. https://doi.org/10.1016/j.tecto.2008.09.003

Obara, K. (2002). Nonvolcanic deep tremor associated with subduction in southwest Japan. *Science*, *296*(5573), 1679–1681. https://doi.org/10.1126/science.1070378

Obara, K., Hirose, H., Yamamizu, F., & Kasahara, K. (2004). Episodic slow slip events accompanied by non-volcanic tremors in southwest Japan subduction zone. *Geophysical Research Letters*, *31*(23), L23602. https://doi.org/10.1029/2004GL020848

Ohmori, K., Taira, A., Tokuyama, H., Sakaguchi, A., Okamura, M., & Aihara, A. (1997). Paleothermal structure of the Shimanto accretionary prism, Shikoku, Japan: Role of an out-of-sequence thrust. *Geology*, *25*(4), 327–330. https://doi.org/10.1130/0091-7613(1997)025<0327:psotsa>2.3.co;2

Oleskevich, D. A., Hyndman, R. D., & Wang, K. (1999). The updip and downdip limits to great subduction earthquakes: Thermal and structural models of Cascadia, south Alaska, SW Japan, and Chile. *Journal of Geophysical Research*, *104*(B7), 14965–14992. https://doi.org/10.1029/1999JB900060

Rabinowitz, H. S., Savage, H. M., Skarbek, R. M., Ikari, M. J., Carpenter, B. M., & Collettini, C. (2018). Frictional behavior of input sediments to the Hikurangi Trench, New Zealand. *Geochemistry, Geophysics, Geosystems*, *19*(9), 2973–2990. https://doi.org/10.1029/2018GC007633

Rice, J. R., & Ruina, A. L. (1983). Stability of steady frictional slipping. *Journal of Applied Mechanics*, *50*(2), 343–349. https://doi.org/10.1115/1.3167042

Rimstidt, J. D., & Barnes, H. L. (1980). The kinetics of silica-water reactions. *Geochimica et Cosmochimica Acta*, *44*(11), 1683–1699. https://doi.org/10.1016/0016-7037(80)90220-3

Roesner, A., Ikari, M. J., Saffer, D. M., Stanislowski, K., Eijsink, A. M., & Kopf, A. J. (2020). Friction experiments under in situ stress reveal unexpected velocity-weakening in Nankai accretionary prism samples. *Earth and Planetary Science Letters*, *538*, 116180. https://doi.org/10.1016/j.epsl.2020.116180

Ruina, A. (1983). Slip instability and state variable friction laws. *Journal of Geophysical Research*, *88*(B12), 10359–10370. https://doi.org/10.1029/jb088ib12p10359

Saffer, D. M., & Marone, C. (2003). Comparison of smectite- and illite-rich gouge frictional properties: Application to the updip limit of the seismogenic zone along subduction megathrusts. *Earth and Planetary Science Letters*, *215*(1–2), 219–235. https://doi.org/10.1016/S0012-821X(03)00424-2

Saffer, D. M., & Wallace, L. M. (2015). The frictional, hydrologic, metamorphic and thermal habitat of shallow slow earthquakes. *Nature Geoscience*, *8*(8), 594–600. https://doi.org/10.1038/ngeo2490

Scholz, C. H. (1998). Earthquakes and friction laws. *Nature*, *391*(6662), 37–42. https://doi.org/10.1038/34097

Schwartz, S. Y., & Rokosky, J. M. (2007). Slow slip events and seismic tremor at circum-Pacific subduction zones. *Reviews of Geophysics*, *45*(3), RG3004. https://doi.org/10.1029/2006RG000208

Segall, P., & Rice, J. R. (1995). Dilatancy, compaction, and slip instability of a fluid-infiltrated fault. *Journal of Geophysical Research*, *100*(B11), 22155–22171. https://doi.org/10.1029/95jb02403

Shibazaki, B., & Shimamoto, T. (2007). Modeling of short-interval silent slip events in deeper subduction interfaces considering the frictional properties at the unstable-stable transition regime. *Geophysical Journal International*, *171*(1), 191–205. https://doi.org/10.1111/j.1365-246X.2007.03434.x

Shreedharan, S., Ikari, M., Wood, C., Saffer, D., Wallace, L., & Marone, C. (2022). Frictional and lithological controls on shallow slow slip at the Northern Hikurangi margin. *Geochemistry, Geophysics, Geosystems*, *23*(2), e2021GC010107. https://doi.org/10.1029/2021GC010107

Skarbek, R. M., & Savage, H. M. (2019). RSFit3000: A MATLAB GUI-based program for determining rate and state frictional parameters from experimental data. *Geosphere*, *15*(5), 1665–1676. https://doi.org/10.1130/ges02122.1

Spinelli, G. A., & Wang, K. (2009). Links between fluid circulation, temperature, and metamorphism in subducting slabs. *Geophysical Research Letters*, *36*(13), L13302. https://doi.org/10.1029/2009gl038706

Sugioka, H., Okamoto, T., Nakamura, T., Ishihara, Y., Ito, A., Obana, K., et al. (2012). Tsunamigenic potential of the shallow subduction plate boundary inferred from slow seismic slip. *Nature Geoscience*, *5*(6), 414–418. https://doi.org/10.1038/ngeo1466

Takahashi, M., Azuma, S., Ito, H., Kanagawa, K., & Inoue, A. (2014). Frictional properties of the shallow Nankai Trough accretionary sediments dependent on the content of clay minerals. *Earth Planets and Space*, *66*(1), 75. https://doi.org/10.1186/1880-5981-66-75

To, A., Obana, K., Sugioka, H., Araki, E., Takahashi, N., & Fukao, Y. (2015). Small size very low-frequency earthquakes in the Nankai accretionary prism, following the 2011 Tohoku-Oki earthquake. *Physics of the Earth and Planetary Interiors*, *245*, 40–51. https://doi.org/10.1016/j.pepi.2015.04.007

Trütner, S., Hüpers, A., Ikari, M. J., Yamaguchi, A., & Kopf, A. J. (2015). Lithification facilitates frictional instability in argillaceous subduction zone sediments. *Tectonophysics*, *665*, 177–185. https://doi.org/10.1016/j.tecto.2015.10.004

Tsutsumi, A., Fabbri, O., Karpoff, A. M., Ujiie, K., & Tsujimoto, A. (2011). Friction velocity dependence of clay-rich fault material along a megasplay fault in the Nankai subduction zone at intermediate to high velocities. *Geophysical Research Letters*, *38*(19), L19301. https://doi.org/10.1029/2011GL049314

Ujiie, K., & Tsutsumi, A. (2010). High-velocity frictional properties of clay-rich fault gouge in a megasplay fault zone, Nankai subduction zone. *Geophysical Research Letters*, *37*(24), L24310. https://doi.org/10.1029/2010gl046002

Underwood, M. B., Basu, N., Steurer, J., & Udas, S. (2003). Data report: Normalization factors for semiquantitative X-ray diffraction analysis, with application to DSDP Site 297, Shikoku Basin. In H. Mikada, G. F. Moore, A. Taira, K. Becker, J. C. Moore, & A. Klaus (Eds.), *Ocean drilling program scientific results* (pp. 190–196).

Valdez, R. D., Kitajima, H., & Saffer, D. M. (2019). Effects of temperature on the frictional behavior of material from the Alpine Fault Zone, New Zealand. *Tectonophysics*, *762*, 17–27. https://doi.org/10.1016/j.tecto.2019.04.022

Wallace, L. M., Webb, S. C., Ito, Y., Mochizuki, K., Hino, R., Henrys, S., et al. (2016). Slow slip near the trench at the Hikurangi subduction zone, New Zealand. *Science*, *352*(6286), 701–704. https://doi.org/10.1126/science.aaf2349

References From the Supporting Information

Underwood, M. B., Laughland, M. M., Byrne, T., Hibbard, J. P., & Ditullio, L. (1992). Thermal evolution of the Tertiary Shimanto Belt, Muroto Peninsula, Shikoku, Japan. *Island Arc*, *1*, 116–132. https://doi.org/10.1111/j.1440-1738.1992.tb00064.x